A&A 366, 636–650 (2001)
DOI: 10.1051/0004-6361:20000292

Astronomy & Astrophysics

Quantification of molecular cloud structure using the Δ-variance

F. Bensch, J. Stutzki, and V. Ossenkopf

I. Physikalisches Institut der Universität zu Köln, Zülpicher Straße 77, 50937 Köln, Germany

Received 4 September 2000 / Accepted 7 November 2000

Abstract. We present a detailed study of the Δ-variance as a method to quantify molecular cloud structure. The Δ-variance was introduced by Stutzki et al. (1998) to analyze the drift behaviour of scalar functions and is used to characterize the spatial structure of observed molecular cloud images. For *fractional Brownian motion structures* (*fBm-fractals*), characterized by a power law power spectrum and random phases, the Δ-variance allows to determine the power spectral index β. We present algorithms to determine the Δ-variance for discretely sampled maps and study the influence of white noise, beam smoothing and the finite spatial extent of the maps. We find that for images with $\beta > 3$, edge effects can bias the structure parameters when determined by means of a Fourier transform analysis. In contrast, the Δ-variance provides a reliable estimate for the spectral index β, if determined in the spatial domain. The effects of noise and beam smoothing are analytically represented in a leading order approximation. This allows to use the Δ-variance of observed maps even at scales where the influence of both effects becomes significant, allowing to derive the spectral index β over a wider range and thus more reliably than possible otherwise. The Δ-variance is applied to velocity integrated spectral line maps of several clouds observed in rotational transitions of ^{12}CO and ^{13}CO. We find that the spatial structure of the emission is well characterized by a power law power spectrum in all cases. For linear scales larger than ∼0.5 pc the spectral index is remarkably uniform for the different clouds and transitions observed ($2.5 \leq \beta \leq 2.8$). Significantly larger values ($\beta \gtrsim 3$) are found for observations made with higher linear resolution toward the molecular cloud MCLD 123.5+24.9 in the Polaris Flare, indicating a smoother spatial structure of the emission at small scales (<0.5 pc).

Key words. interstellar medium (ISM): clouds – ISM: structure – ISM: individual objects: polaris flare – turbulence – methods: data analysis

1. Introduction

Maps of the interstellar medium (ISM) observed in various tracers (e.g. atomic and molecular line transitions, infrared and radio continuum emission, dust extinction maps) show a complex spatial distribution of the emission with a large intensity contrast. This is observed over a wide range in linear resolution, from $\gtrsim$ 50 pc, the extent of giant molecular clouds (or beyond in case of HI observations, cf. Stanimirovic et al. 1999), down to subparsec scales (cf. Zimmermann & Stutzki 1992; Langer et al. 1995; Falgarone & Phillips 1996; Falgarone et al. 1998). Each step towards a higher spatial resolution shows more details and provides evidence of yet unresolved substructure (cf. Scalo 1990; Falgarone et al. 1991; Stutzki 1999; Williams et al. 2000).

For a detailed understanding of the physical processes governing molecular cloud structure, and hence the molecular cloud evolution, a quantitative description of the structure is needed. The quantitative description of the 3-dimensional density and velocity structure is complicated because of the limited information provided by astronomical observations, and cannot be done without additional assumptions. Under the simplifying assumption of homogeneous excitation conditions throughout the cloud, the integrated intensity observed for an optically thin tracer gives the density distribution projected onto the plane of the sky (column density). The line of sight component of the velocity field is accessible by spectral line observations. However, neither the 3-dimensional density distribution nor the other two velocity components are observable. Moreover, the assumption of homogeneous excitation conditions often oversimplifies the situation in molecular clouds, and a potentially significant complication arises from optical depth effects. The limited spatial extent of the observed maps, their finite resolution and the signal-to-noise ratio are additional obstacles on the way towards a quantitative characterization of the observed structure.

Nonetheless, a reliable quantification is needed to compare the structure for different clouds (e.g. quiescent, star-forming), and observed images to images generated using numerical simulations of physical processes (e.g. magneto-hydrodynamic turbulence; cf. Padoan et al. 1998; MacLow & Ossenkopf 2000). This will help to identify the relevant

Send offprint requests to: F. Bensch,
e-mail: bensch@ph1.uni-koeln.de

processes at the different stages of molecular cloud evolution, and thus of star formation.

Over the past decades, several methods have been applied to quantify the structure in observed maps and simulated data. These include the two-point correlation function (autocorrelation and structure function, cf. Scalo 1984; Kleiner & Dickman 1984; Perault et al. 1986; Miesch & Bally 1994), spectral correlation function (Rosolowsky et al. 1999), power spectrum analysis (cf. Crovisier & Dickey 1983; Green 1993), and methods to determine the area perimeter fractal dimension (cf. Beech 1986; Falgarone et al. 1991; Zimmermann & Stutzki 1993; Vogelaar & Wakker 1994). A different approach to quantify the structure is the decomposition of the observed emission into discrete entities ("clumps") in order to establish scaling relations for the clumps (e.g. mass-size relation and clump mass spectra; cf. Stutzki & Güsten 1990; Williams et al. 1994; Kramer et al. 1998; Heyer & Terebey 1998). More recently, Elmegreen & Falgarone (1996) and Stutzki et al. (1998, hereafter Paper I) established links between the fractal dimension and the clump mass and size spectra.

Here, we present a detailed study of the Δ-variance, introduced in Paper I as a new method to quantify the drift behaviour of a 2-dimensional intensity distribution, such as the velocity integrated spectral line maps observed in CO. For images with a power law power spectrum, the Δ-variance allows to determine the spectral index β. Contrary to the power spectrum, the Δ-variance can be determined purely in the spatial domain. This is of potential benefit if the size of the observed, discretely sampled map is smaller than the spatial extent of the emission for a given rms noise level. In this case, the (discrete) Fourier transform of the observed map may be a poor estimate of the Fourier transform of the underlying (continuous) intensity distribution. The truncation of the intensity distribution due to the finite map size gives rise to Fourier amplitudes at high spatial frequencies. The implicitly assumed wrap-around periodicity of the discrete Fourier transform then leads to aliasing, i.e. the high frequency tail of the Fourier transform appears at lower frequencies.

We present algorithms to determine the Δ-variance both in the Fourier and in the spatial domain and compare them with respect to their accuracy and reliability using simulated data. This includes a treatment of the influence of white noise, the telescope beam size, and the "edge effects" arising from the finite image size. Because of the limited number of pixels in typical molecular spectral line maps (the limited dynamical range in angular resolution), these effects modify and possibly even dominate the structural parameters derived (see also Houlahan & Scalo 1990; Miesch & Bally 1994). We show that the Δ-variance is well suited to quantify the structure of observed maps because it is sufficiently robust with respect to these effects.

Section 2 recalls the definition of the Δ-variance and the relation between the Δ-variance and the power spectrum. In Sect. 3 we introduce and compare algorithms to determine the Δ-variance for discretely sampled maps in the Fourier domain and in the spatial domain. They are applied to simulated data to determine their accuracy and to study the influence of edge effects (Sect. 4). The Δ-variance of noisy data and the influence of the telescope beam are considered in Sect. 5, and the Δ-variance of observed molecular spectral line images is presented in Sect. 6. A summary is given in Sect. 7.

2. Definitions and basic relations

The Δ-variance follows the concept of the Allan-variance, originally introduced by Allan (1966) to study the stability of atomic clocks (1-dimensional functions). It provides an extension to functions in higher dimensions and can be applied to images and 3-dimensional structures. Here, we recall some basic relations for functions in two dimensions which are relevant for the following discussion.

Consider a 2-dimensional scalar function $s = s(x, y)$ with x and y representing continuous Cartesian coordinates. Because we are mainly interested in spatial intensity distributions we refer to $s(x, y)$ as an "image". For the sake of simplicity we assume a vanishing average, $\langle s \rangle_{x,y} \equiv 0$. This is no essential restriction and can always be achieved by adding a constant. The Δ-variance is defined as the variance of the convolved image,

$$\sigma_\Delta^2(L) = \frac{1}{2\pi} \langle (s * \bigodot_L)^2 \rangle_{x,y}, \tag{1}$$

where

$$\bigodot_L(r) = \begin{cases} \frac{1}{\pi(L/2)^2} & (r \le \frac{L}{2}) \\ \frac{-1}{8\pi(L/2)^2} & (\frac{L}{2} < r \le \frac{3L}{2}) \\ 0 & (r > \frac{3L}{2}) \end{cases},$$

is an axially symmetric filter function of scale L (denoted as *lag*). The "$*$" symbol is used as shorthand notation for convolution, and $r = (x^2 + y^2)^{1/2}$. In addition, we introduce the notation of $\Delta(L, x, y) = s * \bigodot_L$ for the convolved image.

Other choices for the shape of the filter function are possible to define a modified Δ-variance, eg. a circular filter function with different values of the radii, or a square shaped filter function. Additional information on the non-isotropic character of images can be obtained by using not axially-symmetric filter functions. The detailed study of different filter functions is, however, beyond the scope of the present paper. We choose the above definition (following Paper I) because it is the most simple extension of the Allan-variance concept to functions in higher dimensions. It allows a direct comparison to the linear dimensions in the image: the average distance of a point in the inner area to a point in the annulus is $1.12\,L$. Thus, the $\Delta-$variance $\sigma_\Delta^2(L)$ probes the variation of the intensity s over a length close to L.

Using Rayleigh's theorem, Eq. (1) can be written in the Fourier domain. Here, the Δ-variance is the average

of the image power spectrum $P_\mathrm{s} = P_\mathrm{s}(k_x, k_y)$, weighted by the power spectrum of the filter function,

$$\sigma^2_\Delta(L) = \frac{1}{2\pi} \iint P_\mathrm{s} \, |\tilde{\bigodot}_L|^2 \, \mathrm{d}k_x \mathrm{d}k_y. \quad (2)$$

The integration is done for the 2-dimensional spatial frequency, and the tilde symbol indicates Fourier transformed quantities.

The Allan-variance of a 1-dimensional scalar function is closely related to the power spectrum (cf. Barnes et al. 1971) and a similar relationship holds for the Δ-variance. Consider an image s with a power law power spectrum $P_\mathrm{s} \propto k^{-\beta}$ for $k_\mathrm{l} \leq k \leq k_\mathrm{h}$, where $k = (k_x^2 + k_y^2)^{1/2}$ (see Eq. (A.1) in Appendix A). The Δ-variance of s follows a power law $\sigma^2_\Delta(L) \propto L^{d_\Delta}$ with $d_\Delta = \beta - 2$ for lags L within the regime $(2\pi k_\mathrm{h})^{-1} \ll L \ll (2\pi k_\mathrm{l})^{-1}$. This is valid for spectral indices $0 \leq \beta < 6$ (see Paper I for a more detailed discussion; Appendix A gives a summary for the 2-dimensional case).

Here, we consider images with indices $2 \leq \beta \leq 4$ and $\beta = 0$. This covers the range of indices relevant for images of the ISM, including those typically found for observed maps ($2 \lesssim \beta \lesssim 3$; Crovisier & Dickey 1983; Green 1993; Stanimirovic et al. 1999), and white noise ($\beta = 0$), present in every observation at some level.

3. Δ-variance of discretely sampled, finite maps

3.1. Discretely sampled, finite maps

In the following we set up an algorithm which allows to determine the Δ-variance for observed maps (observations at discrete positions with a finite signal-to-noise ratio and resolution, covering a limited area), providing a reliable quantification of the underlying 2-dimensional intensity distribution. We consider $s = s(x, y)$ as the intensity distribution projected on the plane of the sky with continuous rectilinear coordinates x, y. Strictly, we have to consider the intensity distribution $s = s(\theta, \phi)$ in spherical coordinates θ, ϕ and invoke the corresponding formalism to analyze scalar functions in spherical coordinates. This is done e.g. for the analysis of the cosmic microwave background fluctuations (cf. Smoot et al. 1992; Wright et al. 1996; Tegmark 1996; Kogut & Hinshaw 1996). However, except for spatially very extended surveys of nearby giant molecular cloud complexes and HI surveys, the curvature of the angular coordinates can be neglected locally.

Single dish observations of the ISM do not give $s(x, y)$, rather they represent the intensity detected by a telescope with a beam pattern $B = B(x, y)$, sampled at discrete positions (we assume a normalization of $\iint_{-\infty}^{\infty} B \mathrm{d}x \, \mathrm{d}y = 1$). In order to fully recover the spatial information of the beam convolved image, the observations are made with critical (Nyquist) sampling, given by $\Delta x_\mathrm{crit.} = \lambda/(2D)$ for observations with a telescope of diameter D at a wavelength λ. In practice, a sampling of $\Delta x \approx 0.5\theta_\mathrm{mb}$ is often accepted as "fully sampled". The observed intensity is given by the beam convolved intensity distribution, $s_\mathrm{B} = s * B$. Sampled at discrete positions, this gives an array of intensities $I(i, j) = s_\mathrm{B}(x_i, y_j)$ on a regular grid defined by $(x_i, y_j) = (i\,\Delta x, j\,\Delta y)$.

In the following, we assume equidistant spacing in both coordinates, $\Delta x = \Delta y$. The sum of appropriately weighted δ-peaks at the sampling positions allows us to write $I(i, j)$ as a function of continuous coordinates,

$$\begin{aligned} s_\mathrm{B,s}(x, y) &= \sum_{i=-\infty}^{\infty} \sum_{j=-\infty}^{\infty} I(i, j) \delta(x - i\Delta x) \delta(y - j\Delta x) \\ &= s_\mathrm{B}(x, y) \, \frac{1}{\Delta x^2} \mathrm{III}\left(\frac{x}{\Delta x}, \frac{y}{\Delta x}\right). \end{aligned} \quad (3)$$

Here, the subscript B refers to the beam convolved image, while subscript s indicates the discrete sampling. The *Shah* symbol represents the 2-dimensional array of δ-peaks, $\mathrm{III}(x, y) = \sum_{i=-\infty}^{\infty} \sum_{j=-\infty}^{\infty} \delta(x - i)\delta(y - j)$, following the notation of Bracewell (1986). We use this representation of the observed map in Sect. 5 to study the influence of the beam pattern and noise.

The noise is assumed to be completely uncorrelated, represented by

$$s_\mathrm{n,s}(x, y) = \sum_{i=0}^{m} \sum_{j=0}^{n} I_\mathrm{n}(i, j) \delta(x - i\Delta x) \delta(y - j\Delta x), \quad (4)$$

with $\langle I_\mathrm{n} \rangle_{i,j} = 0$ and $\sigma_\mathrm{n}^2 = \langle I_\mathrm{n}^2 \rangle_{i,j}$. This term is added to the discretely sampled, beam convolved image: $s_\mathrm{B,s} + s_\mathrm{n,s}$.

Observed maps are of finite spatial extent (ignoring all-sky surveys). For maps with $m \times n$ pointings, covering an area $a \times b$, this corresponds to a multiplication of the continuous intensity distribution with a 2-dimensional rectangle-function, shifted by $a/2$ in x and $b/2$ in y, $\sqcap(\frac{x}{a} - \frac{1}{2}, \frac{y}{b} - \frac{1}{2}) = \sqcap(\frac{x}{a} - \frac{1}{2}) \cdot \sqcap(\frac{y}{b} - \frac{1}{2})$, where we use the definition of $\sqcap(\xi) = 1$ ($|\xi| \leq 1/2$) and $\sqcap(\xi) = 0$ ($|\xi| > 1/2$) for the rectangle-function.

Altogether, the observed image of finite extent, affected by white noise and the telescope beam reads

$$s_\mathrm{obs} = (s_\mathrm{B,s} + s_\mathrm{n,s}) \sqcap \left(\frac{x}{a} - \frac{1}{2}, \frac{y}{b} - \frac{1}{2}\right). \quad (5)$$

The intent of the structure analysis is to obtain information on the structure of the original intensity distribution, $s(x, y)$, by studying $s_\mathrm{obs}(x, y)$. Thus, the methods applied have to be sufficiently robust with respect to the effects introduced by the noise, sampling and the finite spatial extent of the map. Alternatively, the influence of these effects have to be determined in order to allow for a correction.

The finite extent of observed maps, in particular, has major implications. Discrete Fourier transform implicitly assumes wrap-around periodicity, artificially introducing steps in the intensity distribution for maps which do not trace the full spatial extent of the emission down to zero intensity. While the beam convolved image $s_\mathrm{B,s}$ is band limited, i.e. it has vanishing Fourier amplitudes beyond an upper frequency cutoff because of the convolution with

the beam pattern, the observed image $s_{\rm obs}$ is not: the finite extent of the image (multiplication with a rectangle function) corresponds to a convolution of the Fourier transform with sinc-functions, $ab\,\mathrm{sinc}(a\,k_x)\,\mathrm{sinc}(b\,k_y) = \frac{\sin(a\pi k_x)}{\pi k_x}\frac{\sin(b\pi k_y)}{\pi k_y}$, and additional phase factors giving the position of the rectangle in the spatial domain. This introduces power at high frequencies, resulting from the extended side-lobes of the sinc-function. As a result, the Fourier transform of the observed map potentially is a poor estimate of the Fourier transform of the original image s. This is independent of the particular choice of the filter function used to represent the finite map size. Any other filter function decaying fast enough within one sampling Δx will equally introduce distorting high frequency components in the power spectrum. A quantitative description of the influence introduced by edge effects is given in Sect. 4.2.

3.2. Algorithms to determine the Δ-variance for observed maps

3.2.1. Δ-variance: Fourier domain

In the Fourier domain, the Δ-variance is given by Eq. (2) and one has to calculate the power spectrum of the observed map. For the numerical code we use the general discrete FT equations, not the fast FT algorithm, in order to avoid the otherwise necessary interpolation or zero padding to match the linear dimension of the maps to 2^N. The image power spectrum is then multiplied to the power spectrum of the filter function and the summation is done for all discrete frequencies to give the Δ-variance at lag L. This is repeated for different lags L with $2 \lesssim (L/\Delta x) \lesssim 0.2\min(n,m)$, the typical range which can be used to determine the spectral index β, as shown in Sect. 4.

3.2.2. Δ-variance: Spatial domain

In order to avoid problems related to the edge effects using the FT of the image, we consider a second method where we convolve the observed image and the filter function $\bigodot_L$ in the spatial domain. For Nyquist sampled observations the beam convolved intensity distribution can be recovered for continuous coordinates by interpolation with the sinc-function (e.g. Bracewell 1986). The thus interpolated function is then convolved with the filter function. In general, it is not possible to exactly recover the spatial intensity distribution because the map boundaries result in an intensity distribution which is *not* band limited. Moreover, an interpolation using the sinc function is often avoided because it is numerically too time consuming. Therefore, we use an approximation to the convolution integral and demonstrate that this approach provides reliable results.

Numerically, the convolved image at position x_i, y_j is determined according

$$\Delta(L,i,j) = \sum_{k,l\in\mathrm{circ.}} \alpha(i-k,j-l) I_{\rm obs}(k,l) - \sum_{k,l\in\mathrm{ann.}} \alpha(i-k,j-l) I_{\rm obs}(k,l), \quad (6)$$

with $1 \le i \le m$, $1 \le j \le n$, and $k,l \in \mathbb{N}$. In the first term of the right hand side, the sum is over all positions inside the circle of radius $L/2$, centered on (x_i, y_j). For the second term, the sum is over positions inside the annulus of inner and outer radius $L/2$ and $3L/2$. The $\alpha(i-k,j-l)$ are weighting factors with the normalization $\sum_{\rm circ.}\alpha(i-k,j-l) = \sum_{\rm ann.}\alpha(i-k,j-l) \equiv 1$. We consider two different sets of weighting factors. As a first option we set $\alpha(i-j,k-l) \equiv$ const. within both parts of the filter ("POINT" algorithm, see left panel of Fig. 1). This is equivalent to determining the average intensity of the emission detected towards the positions (x_k, y_l) inside the circle, subtracting the average intensity of the positions in the annulus. As a second option, the weighting factors are determined by the (fraction) of the pixel *area* which is covered by the respective part of the filter function, with the pixels being defined as squares $(\Delta x)^2$ centered on x_i, y_j ("PIX" algorithm, right panel of Fig. 1). The weighting factor is $\alpha(i-k,j-l) \propto (\Delta x)^2$ for pixels entirely inside the circle, and correspondingly smaller if a fraction of the pixel is outside the circle. The same applies to the weighting factors of the pixels covered by the annulus. The summation in Eq. (6) is then done for all pixels which are at least partially covered by the circle or the annulus, respectively.

For both options (POINT and PIX) the question remains how to treat the positions close to the edge of the map where the filter function overlaps the map boundary and the convolution integral is only partly known. One possible option is to exclude those positions, resulting in a smaller area of the map to be used with a larger filter function. The result is then biased because different sub-sets of the image are probed by the Δ-variance at different lags L. In order to avoid this bias we determine the convolved map for all positions (i,j) of the map according Eq. (6), *including* those where the filter function intersects the map boundary. For the latter positions we use weighting factors with a modified normalization: $\sum_{k,l}\alpha(i-k,j-l) \equiv 1$, where the summation is done *only* for those k,l which are inside the circle centered on (x_i, y_j) *and* the observed map. The same is done for the positions covered by the annulus.

The Δ-variance is then computed as the variance of the thus convolved image,

$$\sigma^2_\Delta(L) = \frac{1}{2\pi}\frac{1}{m\,n}\sum_{i=1}^{m}\sum_{j=1}^{n}[\Delta(L,i,j) - \bar{\Delta}(L)]^2, \quad (7)$$

where $\bar{\Delta}(L) = \langle\Delta(L,i,j)\rangle_{i,j}$ is the average of the convolved map. Note, that the Δ-variance in Eq. (7) includes

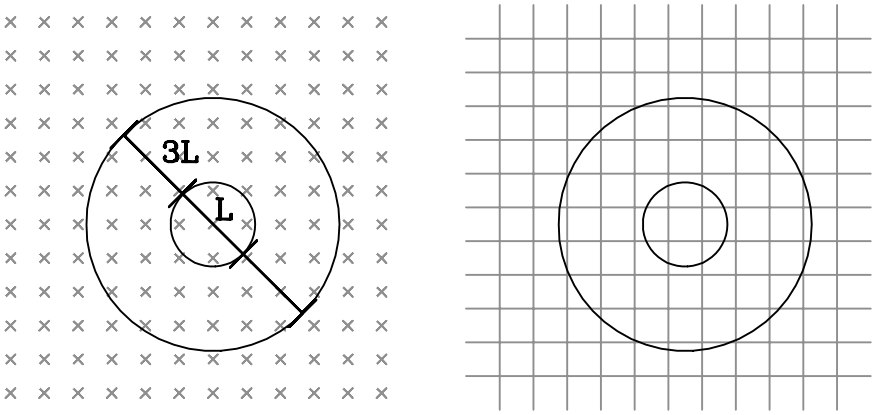

Fig. 1. Convolution of the a discretely sampled map with the cylindric filter function $\bigodot_L$ of linear size L. Illustration of the "POINT" (left panel) and the "PIX" algorithm (right panel)

the subtraction of the average value, which we have previously assumed to be zero. This accounts for the fact that for maps of finite extent and a vanishing average intensity $\langle s \rangle_{x,y} = 0$, the average intensity of the the convolved map $\bar{\Delta}(L)$ not necessarily vanishes, due to the edge effects.

4. Testing the Δ-variance with simulated data

First results of a Δ-variance analysis of observed molecular cloud images are presented in Paper I. These studies suggest that the spatial structure of the velocity integrated spectral line maps is well characterized by a power law power spectrum with a spectral index $\beta \sim 2.8$ and randomly distributed phases of the Fourier amplitudes. Scalar functions with this property are also known as *fractional Brownian motion structures* (*fBm-fractals*, cf. Peitgen & Saupe 1988). Thus, *fBm-fractals* are ideal test images with well known properties, providing a realistic representation of observed molecular cloud images. In particular, they are useful to calibrate algorithms used to quantify the structure in observed ISM images (cf. Vogelaar & Wakker 1994).

4.1. Application to fBm-fractals

For a first test of the algorithms, we generate a set of 2-dimensional *fBm-fractals* with $n^2 = 512 \times 512$ pixels and a power law power spectral index β between 2 and 4 (Fig. 2). The *fBm-fractals* are generated by the Fourier transform of hermitian Fourier amplitudes with randomly distributed phases, giving real valued images. A constant offset is added to the resulting maps to obtain non-negative intensities.

We apply the Δ-variance algorithm in the Fourier domain, and both algorithms in the spatial domain (PIX and POINT). The results for the image with $\beta = 3$ are shown in Fig. 3. Similar results are obtained for the other *fBm-fractals*. Note, that large scale trends and edge effects are absent here, because the *fBm-fractals* are by construction wrap-around periodic.

The Δ-variance follows a power law for lags $2 \lesssim L/\Delta x \lesssim 100$, with a turnover for lags $L/\Delta x$ larger than $100 \approx 0.2\,n$. The turnover results from the low frequency cutoff in the power spectrum (recall, that the power law behaviour of the Δ-variance is limited to lags $(2\pi k_\mathrm{u})^{-1} \ll L \ll (2\pi k_\mathrm{l})^{-1}$). With $k_\mathrm{u} \approx (\Delta x)^{-1}$ and $k_\mathrm{l} \approx (n\,\Delta x)^{-1}$ for maps with n^2 pixels, we conclude that the Δ-variance can be described by a power law for lags $10\,(2\,\pi\,k_\mathrm{u})^{-1} \lesssim L \lesssim (2\,\pi\,k_\mathrm{l})^{-1}$. A fit to the Δ-variance of observed images should be restricted to this range.

A linear fit to the Δ-variance determined in the Fourier domain gives an index of $d_\Delta = 1.00$, exactly matching the value expected for the *fBm-fractal* with $\beta = 3$, $d_\Delta = \beta - 2 = 1$. We obtain an index of 1.05 for the Δ-variance determined in the spatial domain (POINT and PIX option), still reasonably close to 1.

Comparing the results in the spatial domain, we find that the Δ-variance determined using the PIX algorithm is shifted towards smaller σ_Δ^2 (however, with the same power law index d_Δ). The reason is the numerical convolution of the map and the filter function, done for the PIX option. Here, some of the pixels contribute to both, the positive and negative sum in Eq. (6), because they are partially contained in the circle *and* the annulus of the filter function. This introduces correlations for the integrated intensity determined for both parts of the filter function and effectively lowers the variance of the thus convolved map. The scaling properties of the Δ-variance, however, remains unaffected, and it turns out that both algorithms are reliable methods to determine the spectral index β. In the following, we limit the discussion to the POINT method, because of its numerical simplicity.

We have also studied the Δ-variance of the 1-dimensional projection of *fBm-fractals*. With the 1-dimensional projection being a zero-cut in the Fourier domain, the projected image has the same power spectral index β as the original image. The Δ-variance of the 1-dimensional projections follows a power law with a spectral index of $d_\Delta = \beta - 1$ (Paper I). This is confirmed for the projections of the *fBm-fractals* shown in Fig. 2, using an algorithm which determines the Δ-variance in the

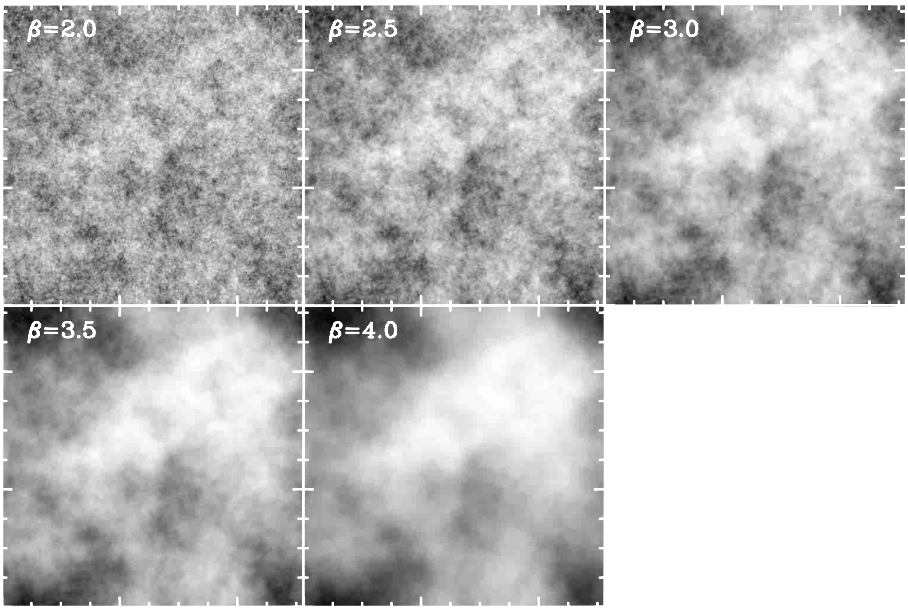

Fig. 2. 2-dimensional *fBm-fractals* with 512 × 512 pixels and a power law power spectral index β between 2.0 and 4.0. An identical phase distribution is used for the images

Fourier domain. Thus, for images with wrap-around symmetry, it is possible to determine the spectral index β by studying their 1-dimensional projections.

4.2. Finite size and edge effects

4.2.1. Theoretical considerations for 2-dimensional *fBm-fractals*

Generally, observed images are not wrap-around periodic. For a quantitative treatment of the thus introduced edge effects we assume an image with a power law power spectrum, $P_{\rm s} \propto k^{-\beta}$, and neglect the influence of the beam pattern, sky and instrumental noise for the moment ($s_{\rm B} = s$ and $s_{\rm n,s} = 0$ in Eq. (5)). The power spectrum of the observed map then reads

$$P_{\rm s_{obs}} \propto k^{-\beta} \; * \; a\,b\,\mathrm{sinc}^2(a\,k_x)\,\mathrm{sinc}^2(b\,k_y) \; * \; [\mathrm{III}(k_x\Delta x, k_y\Delta y)]^2, \quad (8)$$

where we have used that III(x) is its own Fourier transform.

The convolution of the power spectrum $P_{\rm s} \propto k^{-\beta}$ with the sinc-function has major implications for images with $\beta > 2$. Here, the power spectrum of the tapered image decays with $P_{\rm s_{obs}} \propto k^{-2}$ in leading order approximation for large spatial frequencies k, because of the $\propto k^{-2}$ dependency of the squared sinc-function. Only for images with a spectral index $\beta \leq 2$, the $k^{-\beta}$ behaviour of the power spectrum is preserved for large k. In addition, oscillations are introduced for the sinc^2-convolved power spectrum, because of the close cancellation of the squared sin-wave when averaged over an image of finite spatial extent.

Thus, for images with a power law power spectral index larger than 2, we expect a systematic deviation of the spectral index obtained for a sub-set, and thus for the power spectrum of any observed map which does not trace the full spatial extent of the emission.

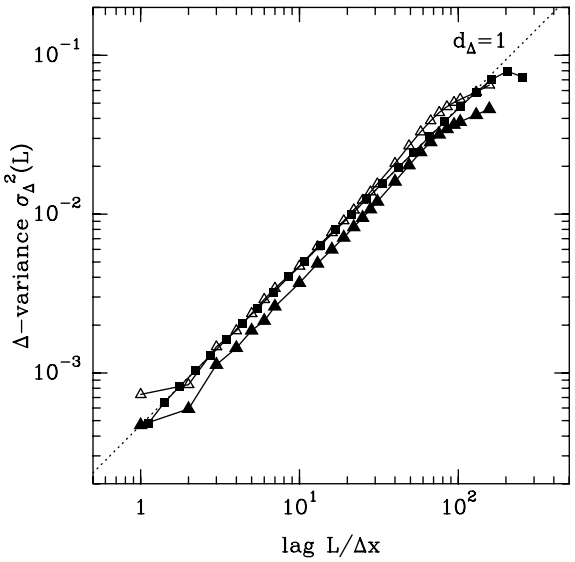

Fig. 3. Δ-variance computed for a *fBm-fractal* with $\beta = 3.0$. The results obtained with the algorithm in the Fourier domain (filled squares) and the algorithms in the spatial domain (POINT, empty triangles, and PIX, filled triangles) are compared. The theory of *fBm-fractals* predicts a power law index of $d_\Delta = \beta - 2 = 1$ for the Δ-variance

4.2.2. Simulations of finite size effects

It is not possible to exactly determine the modifications in the power spectrum introduced by the edge effects. We therefore use numerical simulations for a quantitative estimate. We consider sub-sets with $n \times n$ pixels ($n = 32, 64, 128$) of larger 512 × 512 *fBm-fractals*. The

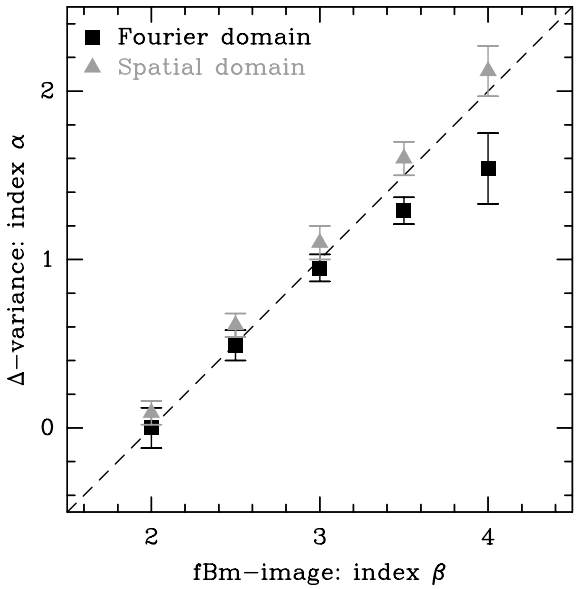

Fig. 4. Index d_Δ of the Δ-variance, determined for sub-sets of *fBm-fractals* (the results for 64×64 sub-sets of *fBm-fractals* with 512×512 pixels are shown). The marker gives the sample average index d_Δ of 10 sub-sets. The sample rms is indicated as error bar. The results obtained with the Δ-variance algorithm in the Fourier domain (dark) and the spatial domain (grey symbols) are compared. The dashed line indicates the relation $d_\Delta = \beta - 2$ for *fBm-fractals*

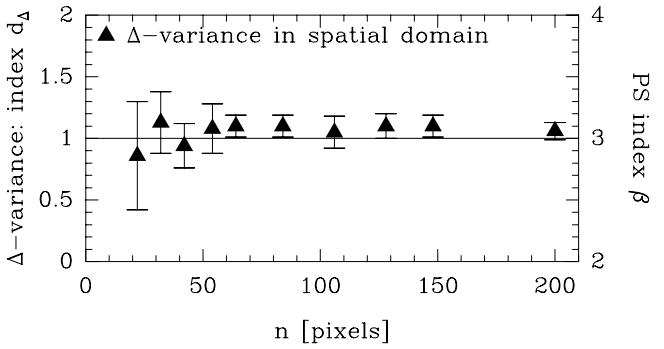

Fig. 5. Power law index d_Δ of the Δ-variance, determined for sub-sets ($n \times n$ pixels) of larger *fBm-fractals* (512×512 pixels; $\beta = 3$). The Δ-variance is determined in the spatial domain, using the POINT algorithm. For each n, a sample of 10 sub-sets is studied. The sample rms of the d_Δ is given as error bar. The horizontal line ($d_\Delta = 1$) indicates the value expected for a *fBm-fractal* with $\beta = 3$

Δ-variance is determined in the Fourier domain and in the spatial domain. To get an error estimate, we generate a sample of 10 *fBm-fractals*, each with the same spectral index β but different initial seeds for the phases. We randomly pick one $n \times n$ sub-set from each *fBm-fractal* and determine the power law index d_Δ of its Δ-variance. The sample average index is used as best estimate for d_Δ, and the sample rms as an estimate for its accuracy. This is done for *fBm-fractals* with $\beta = 2.0, 2.5, 3.0, 3.5$ and 4.0. Figure 4 shows the resulting power law indices d_Δ for sub-sets with $n = 64$.

The sample average index d_Δ obtained from the Δ-variance in the spatial domain follows a linear relation with the spectral index β. However, they are slightly larger (by $\lesssim 0.1$) than expected from the relation $d_\Delta = \beta - 2$. This is marginally significant, because the sample rms typically is 0.10 (0.15 for $\beta = 4$).

For the Δ-variance determined in the Fourier domain, the sample average indices closely follow the relation $d_\Delta = \beta - 2$ only for $\beta \leq 3$. For larger β, the sample average is significantly smaller and the individual indices d_Δ scatter over a wider range, indicated by the larger error bar. Similar results are obtained for larger ($n = 128$) and smaller ($n = 32$) sub-sets. This confirms the results from the previous section, where we have seen that edge effects are significant for maps covering only a fraction of a spatially extended emission. The simulations demonstrate that the difference is small for $2.0 \leq \beta \leq 3.0$ and significant for $\beta > 3$.

We conclude that Fourier transform of the sub-set does not provide a reliable estimate for the Fourier transform of the underlying (continuous) intensity distribution, and thus that Fourier transform algorithm should be avoided for the analysis of observed maps if they do not cover the full spatial extent of the emission.

4.2.3. Accuracy of the power law index for sub-sets of different size

In order to study the accuracy for sub-maps of different size $n \times n$, we repeat the above simulations varying n between 16 and 206. We consider a sample of 10 sub-sets, picked from *fBm-fractals* with $\beta = 3$. The index d_Δ is determined using the Δ-variance algorithm for the spatial domain. Figure 5 shows the sample average index d_Δ as a function of the sub-set size n.

For $n \geq 64$, the sample average of the indices is $\sim$1.1, with a rms of typically $\sim$0.1. The accuracy degrades towards smaller n (the rms increases to $\sim$0.25 for $n = 32$) and steeply increases for maps with $n < 32$. No reliable results are obtained for sub-sets with $n \leq 24$. For the latter, the Δ-variance of at least 3 sub-sets does not follow a simple power law and the indices of the remaining sub-sets scatter over a wide range, resulting in a rms > 0.3. We conclude that maps with at least 32×32 pixels are needed for a reasonable Δ-variance analysis.

Eye inspection of the results show that the Δ-variance typically follows a power law for lags $2 \lesssim L/\Delta x \lesssim 0.2\,n$, with only few exceptions (typically, 1 out of 10). For $n = 24$, this translates to a range $2 \lesssim L/\Delta \lesssim 6$ with only 2 to 3 independent measurements of the Δ-variance. This is too small to obtain the power spectral index with a reasonable accuracy and confirms our result that maps with at least 32×32 pixels are needed for an analysis.

Tests for *fBm-fractals* with different indices $\beta = 2.0, 2.5, 3.5, 4.0$ show that the sample rms index depends only weakly on β, typically being 0.10 for $n \geq 64$ and 0.20

Table 1. Spectral index $\beta = d_\Delta + 2$, determined for a sample of 10 sub-sets of *fBm-images*. Prior to the Δ-variance analysis, large scale trends were removed with the subtraction of a bilinear surface, $I(x,y) = a\,x + b\,y + c\,xy + d$, or a planar surface, $I(x,y) = a\,x + b\,y + d$, fitted to the image (with a, b, c, d being the parameters to be fitted). Alternatively, a symmetrized version of the maps is considered. The results obtained for the original maps are given in the last row

method	power law power spectral index β of *fBm-fractal*				
	2.0	2.5	3.0	3.5	4.0
bilinear surface	2.10 ± 0.05	2.63 ± 0.10	3.07 ± 0.08	3.59 ± 0.14	3.95 ± 0.14
planar surface	2.12 ± 0.06	2.62 ± 0.08	3.10 ± 0.11	3.52 ± 0.22	4.03 ± 0.15
symmetrized	2.11 ± 0.16	2.66 ± 0.09	3.17 ± 0.12	3.60 ± 0.20	4.13 ± 0.19
unmodified	2.05 ± 0.14	2.66 ± 0.08	3.18 ± 0.12	3.65 ± 0.25	4.11 ± 0.15

for $n = 32$. The exception is $\beta = 4$ where the accuracy varies between 0.15 ($n \geq 64$) and 0.25 ($n = 32$).

4.2.4. Subtraction of large scale trends

Here, we investigate ways to further reduce the influence of the edge effects by subtracting large-scale, systematic trends. These large-scale trends can appear because of the particular size and position of a the map covering a fraction of a spatially more extended intensity distribution. Structure which is random on larger scales can appear as a systematic trend in the sub-map, for instance, as a gradient.

In all previous computations a bilinear surface is fitted and subtracted from the sub-maps prior to the Δ-variance analysis. This is now repeated using a planar surface instead. Alternatively, we generate a symmetrized version of the map with its mirror images along the x and y-axis added. Table 1 compares the results to those obtained for the original maps.

Generally, the results obtained with the different methods do not substantially differ from each other. The sample average indices agree within the rms. However, the results obtained with a prior fit and subtraction of a bilinear surface and a planar surface are slightly closer to the d_Δ expected for the original *fBm-fractal*, and we use these two options for the analysis of observed data.

5. Influence of white noise and the telescope beam

The influence of noise and the telescope beam pattern modify the spatial structure of the observed emission predominantly at small linear scales, close to the sampling for fully sampled observations. While the beam convolution artificially introduces correlations, the noise effectively reduces existing ones. As a result, the Δ-variance of *fBm-fractals* deviates from the expected power law behaviour toward smaller lags. In general, an exact correction for both effects is not possible. For images with a power law power spectrum, however, their influence can be approximated.

5.1. Δ-variance of images with a finite signal-to-noise ratio

In order to give an example, we added white noise to the *fBm-fractal* shown in Fig. 2 ($\beta = 3$). The resulting image is shown in the upper panel of Fig. 6. The signal-to-noise ratio is $S/N = 1.6$, where we use the definition of $S/N = \sigma_\beta/\sigma_\mathrm{n} = (\langle(s_\beta - \bar{s}_\beta)^2\rangle/\langle s_\mathrm{n}^2\rangle)^{1/2}$, the ratio of the rms of the *fBm-fractal* and the rms of the white noise. Note, that this is different from the S/N-ratio used for observed data, commonly defined as the ratio between the maximum (or some other representative value of the intensity in the map) to the rms noise of the signal-free pixels. For simulated data generated by a stochastic process, the intensity maximum depends on the number of pixels in the map and thus is not useful for a definition of the S/N-ratio.

The lower panel of Fig. 6 shows the Δ-variance of the same *fBm-fractal* at different noise levels. The white noise becomes increasingly important towards smaller scales, resulting in a larger Δ-variance. For S/N-ratios $\lesssim$10, the Δ-variance exhibits a turnover, approaching the L^{-2} behaviour of pure white noise.

For a quantification we consider images s_β with a power law power spectrum $P_{\mathrm{s}_\beta}(k) = P_{\mathrm{s}_\beta,0}\,k^{-\beta}$, and white noise with a flat power spectrum $P_{\mathrm{s_n}}(k) = P_{\mathrm{s_n},0}\,k^0$, $k_\mathrm{l} \leq k \leq k_\mathrm{h}$. The constants P_{0,s_β} and $P_{0,\mathrm{s_n}}$ are determined by the integral over the power spectrum, $\sigma_\beta^2 = \iint P_{\mathrm{s}_\beta}\,\mathrm{d}k_x\mathrm{d}k_y$ and $\sigma_\mathrm{n}^2 = \iint P_{\mathrm{s_n}}\,\mathrm{d}k_x\mathrm{d}k_y$. The power spectrum of the noisy image $s = s_\beta + s_\mathrm{n}$ is then approximated by

$$P_\mathrm{s} \approx P_{\mathrm{s}_\beta} + P_{\mathrm{s_n}} = P_{0,\mathrm{s}_\beta} k^{-\beta} + P_{0,\mathrm{s_n}}. \quad (9)$$

Note that the cross terms containing the product of the *fBm-fractal* and the white noise Fourier transform are neglected. For images of infinite spatial extent they vanish on average, because the phases of the Fourier transform are uncorrelated.

The assumption of white noise is appropriate for most of the observed radio spectral line maps. However, the results do not significantly change if we consider non-uniform noise instead, where the rms is a function of the position in the map (e.g. scaling with some function of the observed intensity, such as the square root of the intensity, applicable if Shot-noise dominates). The crucial point

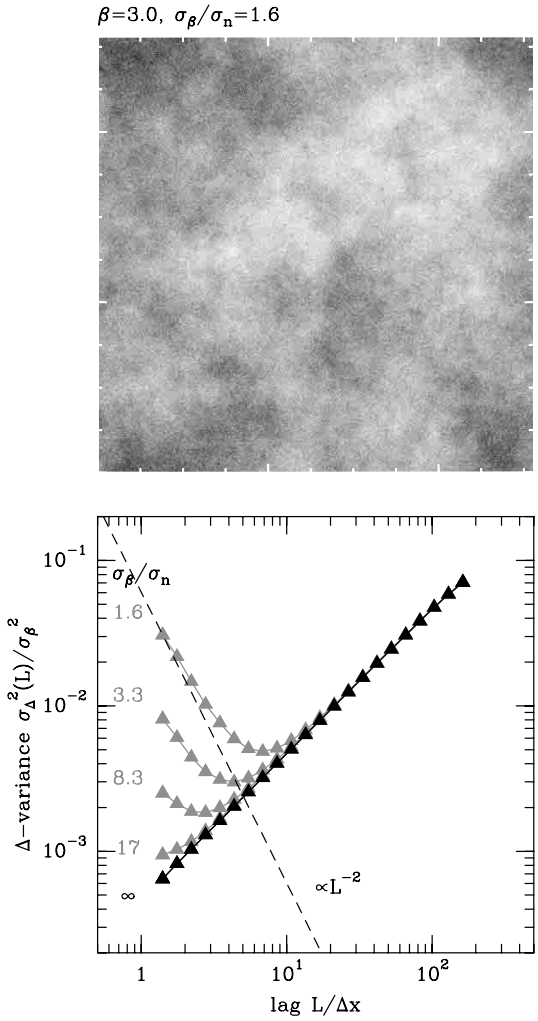

Fig. 6. *fBm-fractal* with white noise added (top). The *fBm-fractal* is the one shown in Fig. 2 with $\beta = 3$. The bottom panel shows the Δ-variance of the same *fBm-fractal* at different noise levels. The broken line indicates $\sigma^2_\Delta(L) \propto L^{-2}$, the Δ-variance of pure white noise. Note, that we define the signal-to-noise ratio as the rms of the *fBm-fractal* to the rms of the white noise, $\sigma_\beta/\sigma_\mathrm{n}$

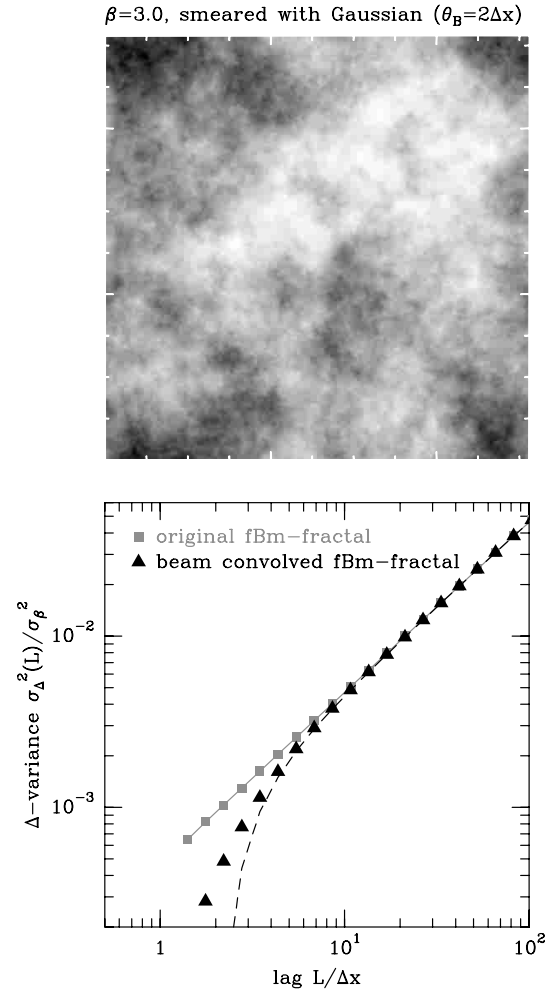

Fig. 7. Top panel: *fBm-fractal* ($\beta = 3$), convolved with a Gaussian beam of HPBW twice the sampling. The corresponding Δ-variance is shown by the dark triangles in the bottom panel. The Δ-variance of the original *fBm-fractal* is given by grey squares, and the approximation deduced for the Δ-variance of the beam convolved image is indicated by the broken line

is that the phases of the image and noise Fourier transform are completely uncorrelated. In this case we can assume that the contribution of the cross terms in the power spectrum P_s vanish on average, and thus that it can be neglected for the Δ-variance.

For discretely sampled maps of finite spatial extent, however, the cross terms may not exactly cancel. This applies even if we assume pure white noise. The power spectrum then follows Eq. (9) only on average, with additional random fluctuations due to the near cancellation of the cross terms. Similar fluctuations are present in the Δ-variance.

From Eq. (2) it is evident that calculating the Δ-variance is a linear operation on the power spectrum. The Δ-variance of the noisy image is therefore approximated by

$$\sigma^2_\Delta(L) \approx a_1 L^{\beta-2} + a_2 L^{-2}, \tag{10}$$

for lags $(2\pi k_\mathrm{h})^{-1} \ll L \ll (2\pi k_\mathrm{l})^{-1}$. The constants are given by $a_1 = \sigma^2_\beta c_\beta (2\pi k_\mathrm{l})^{\beta-2}$ and $a_2 = \sigma^2_\mathrm{n} \frac{9}{4\pi^3} k_\mathrm{h}^{-2}$, with the c_β from Table A1 in Appendix A.

5.2. Influence of the finite telescope beam

For a quantitative treatment we consider a telescope beam of Gaussian profile and HPBW θ_mb. The beam convolved image is then given by

$$s_\mathrm{B} = s_\beta * \left(\frac{4\ln 2}{\pi\theta^2_\mathrm{mb}}\right) \exp\left[-4\ln 2\left(\frac{x^2+y^2}{\theta^2_\mathrm{mb}}\right)\right]. \tag{11}$$

A beam convolved *fBm-fractal* ($\beta = 3$) is shown as an example in the upper panel of Fig. 7, where the HPBW of the Gaussian is twice the sampling. In the lower panel, the Δ-variance of the original and the convolved image are compared. Clearly, the influence of the finite beam size is noticeable for lags up to $(L/\Delta x) \sim 8$, and a linear fit to

the Δ-variance has to be limited to larger lags. This might be a problem for observed maps because of their limited dynamical range in linear resolution, often little more than one decade. A quantitative description is therefore highly desirable in order to extend the fit to smaller lags, and to evaluate the Δ-variance for smaller maps.

The power spectrum of the beam convolved *fBm-fractal* is

$$P_{\rm B}(k) \propto k^{-\beta} \exp\left[-\frac{\pi^2\theta_{\rm B}^2}{2\ln 2}k^2\right].$$

Series expansion for the Gaussian gives

$$P_{\rm B}(k) \propto k^{-\beta} - \frac{\pi^2\theta_{\rm B}^2}{2\ln 2}\, k^{-\beta+2} + \mathcal{O}(k^{-\beta+4}) + \cdots \qquad (12)$$

For small k, the influence of the beam is approximated by an additive term $\propto k^{-\beta+2}$. An approximation to the Δ-variance of the beam convolved image for large lags $L \gg \theta_{\rm mb}(8\ln 2)^{-1/2}$ is then given by (Appendix B),

$$\sigma'^2_\Delta(L) \approx \sigma^2_\Delta(L)\left[1 - K_\beta\left(\frac{L}{\theta_{\rm mb}}\right)^{-2}\right], \qquad (13)$$

where $\sigma^2_\Delta(L) = \sigma^2_\beta c_\beta (2\pi k_{\rm l} L)^{\beta-2}$ is the Δ-variance of the original image and $[1+K_\beta(L/\theta_{\rm mb})^{-2}]$ gives a leading order correction for the influence of the Gaussian beam. K_β is a function of the index β and the low (high) frequency cutoff, $k_{\rm l}, k_{\rm h}$ (Appendix B). This approximation is shown in the lower panel of Fig. 7 by the broken line.

Additional correction using higher order terms of the series expansion in Eq. (12) is not possible. The next term is $\propto k^{-\beta+4}$, and for the $2 \le \beta \le 4$ considered here, this term has an exponent between −2 and 0. The corresponding Δ-variance does no longer follow a power law.

6. Application to observations

6.1. Observed CO spectral line maps

We applied the Δ-variance algorithm to a sample of 10 spectral line maps, observed in the rotational transitions of CO. The data set contains 5 maps made with different angular resolution toward the Polaris Flare, a high latitude translucent cloud close to the North Celestial Pole. It is a quiescent cloud with no embedded stars or ongoing star formation (see, however, Heithausen 1999). The distance estimates range from 100 pc to 250 pc (cf. Heithausen & Thaddeus 1990; Zagury et al. 1999). Here, we adopt a distance of $d = 150$ pc. The Polaris Flare data set includes the survey of the entire cloud complex in the ^{12}CO $J = 1 \rightarrow 0$ transition (angular resolution of 8.7 arcmin; Heithausen & Thaddeus 1990). For one of the cores, MCLD 123.5+24.9, observations were made with the KOSMA 3 m (Bensch 1998) and the FCRAO 14 m telescope (at 2.2 and 0.78 arcmin resolution). In addition, CO observations made at very high angular resolution (0.35 and 0.175 arcmin) are available with the maps of the IRAM key-project "*small-scale structure of pre-star-forming regions*" (Falgarone et al. 1998). Taken together, the observed maps cover more than three decades in linear resolution, from ∼50 pc to ∼0.008 pc (Table 2).

In addition, we applied the Δ-variance to molecular cloud surveys made with the AT&T Bell Labs 7 m telescope in the ^{13}CO $J = 1 \rightarrow 0$ transition. They are provided by J. Bally (*priv. comm.*; see also Bally et al. 1987, Bally et al. 1989, and Miesch & Bally 1994). A summary of the observations and the results of the Δ-variance analysis are given in Table 3.

6.2. Δ-variance analysis of the velocity integrated maps

Prior to the Δ-variance analysis, a bilinear surface is fitted and subtracted from those maps which do not cover the full extent of the emission (the MCLD 123.5+24.9 maps made with the KOSMA and IRAM telescope). The Δ-variance is determined using the POINT algorithm and the accuracy is estimated as the statistical error,

$$\Delta(\sigma^2_\Delta(L)) = \left\langle \left([\Delta(L,k,l) - \bar{\Delta}(L)]^2 - \sigma^2_\Delta(L) \right)^2 \right\rangle_{k,l}, \qquad (14)$$

represented in Figs. 9 and 10 by error bars. Here, k and l sample positions separated by L ($1 \le k \le \frac{m}{L}$ and $1 \le l \le \frac{n}{L}$) to obtain a set of independent intensities of the squared convolved map, $(\Delta(L,k,l) - \bar{\Delta}(L))^2$. This gives an upper limit to the actual error because the variations in the convolved map only partly result from the limited accuracy, but also reflect source intrinsic properties. However, it provides the correct relative accuracy of the Δ-variance at different lags, and thus the proper weighting for the fit. The accuracy of the Δ-variance is better at smaller lags because of the larger number of independent positions available in the convolved map. For larger lags, a larger fraction of the convolved map is affected by edge effects, and the variation of the intensity in the convolved map (Eq. (14)) provides a reasonable upper limit to the error.

According to the equation deduced in Sect. 5 for the Δ-variance of beam convolved, noisy images we applied a three-parameter χ^2-fit to the resulting Δ-variance,

$$\sigma^2_\Delta(L) = a_1\,(1 - K_\beta(L/\theta_{\rm mb})^{-2})\,L^{\beta-2} + a_2\,L^{-2}, \qquad (15)$$

where a_1, a_2 and $\beta = d_\Delta + 2$ are the parameters to be fitted. K_β includes integrals of Bessel functions. Therefore, it is not possible to write K_β in a closed form and we use the second order polynomial $K_\beta \approx 3.9159 - 1.2437\,\beta + 0.1189\,\beta^2$ as an approximation. This is obtained from a fit to 20 values of K_β, evaluated numerically for β between 2.1 and 3.9, and the additional assumption of $\frac{1-(k_{\rm l}/k_{\rm h})^{4-\beta}}{1-(k_{\rm l}/k_{\rm h})^{\beta-2}} \approx 1$.

The thus obtained spectral indices β are given in the second last column of Tables 2 and 3. The error is the standard deviation of the fit parameter β, with the error due to the finite size of the map (Sect. 4.2.3) added in quadrature.

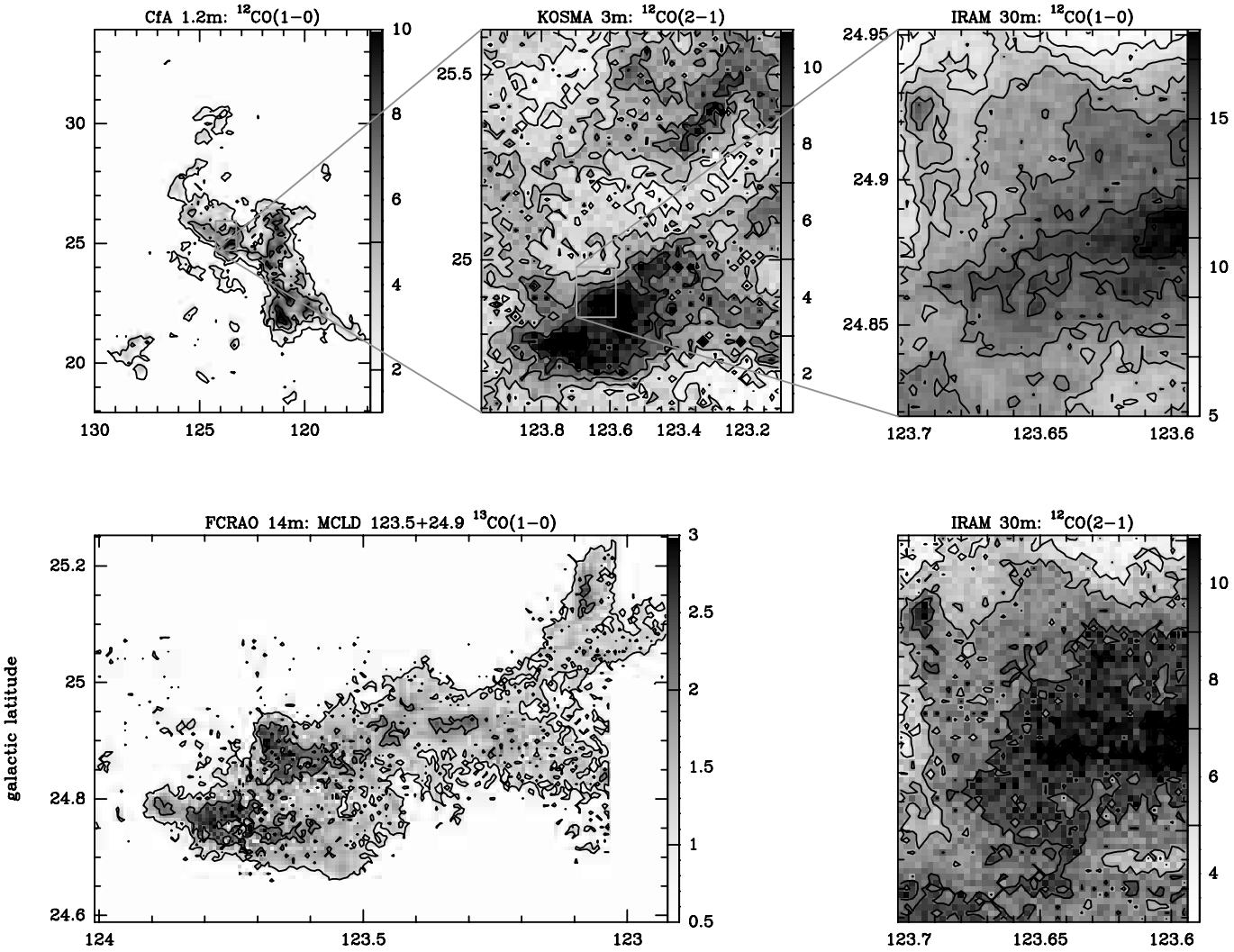

Fig. 8. Velocity integrated spectral line maps of the rotational transition ^{12}CO $J = 1 \rightarrow 0$, ^{12}CO $J = 2 \rightarrow 1$ and ^{13}CO $J = 1 \rightarrow 0$, observed towards the Polaris Flare, and one of its cores, MCLD 123.5+24.9. The transition and the telescope are indicated at the top of each panel. The line intensity is given in main beam brightness temperature, $T_{\rm mb}$. Iso-intensity levels are shown from 2 to 8 in steps of 2 (CfA map), 1 to 11 by 2 (KOSMA), 1 to 4 by 1 (FCRAO), 5 to 17 by 2 (IRAM, ^{12}CO $J = 1 \rightarrow 0$), 3 to 11 by 2 (IRAM, ^{12}CO $J = 2 \rightarrow 1$), in units of K km s^{-1}

6.3. Results

The power spectral indices obtained for the large surveys (CfA map of the Polaris Flare and the Bell 7 m surveys) cover a remarkably narrow range, between 2.5 and 2.8. The only exception is the ^{13}CO $J = 1 \rightarrow 0$ map of Perseus/NGC 1333 with a steeper index of $\beta = 3.07 \pm 0.10$. The maps observed with higher angular resolution toward MCLD 123.5+24.9 give significantly larger indices $\beta > 3$. This indicates that the spatial structure of the intensity distribution is smoother at linear scales $\lesssim 0.5$ pc. The result obtained for the Perseus/NGC 1333 ^{13}CO $J = 1 \rightarrow 0$ map fits into this picture. The distance to the cloud is 350 pc, smaller than for any of the other clouds in the Bell Labs sample. This allows to probe smaller linear scales than accessible with the other maps.

Note, that a Δ-variance of the ^{12}CO $J = 1 \rightarrow 0$ maps made with the CfA 1.2 m and the IRAM 30 m telescope are also presented in Paper I, giving $\beta = 2.77$ and $\beta = 2.76$. For this analysis we used the FT algorithm to determine the Δ-variance. While the index β of the CfA map is in close agreement with the result obtained here, the index determined in Paper I for the IRAM map is significantly smaller. We attribute this to the influence of edge effects, which are obviously relevant for the IRAM maps.

In order to demonstrate the influence of white noise and beam smearing, the Δ-variance of the beam convolved image *without* the contribution of the white noise is marked by dashed lines in Fig. 9. The difference between the dashed and the solid lines illustrates the influence of the white noise and the divergence of the dashed line from a straight line (not shown) indicates the influence of the beam smearing. Both, the white noise and beam smearing, significantly modify the Δ-variance. For instance, if we neglect them by fitting a straight line to the

Table 2. Observations of CO rotational transitions made towards the Polaris Flare and MCLD 123.5+24.9. The Δ-variance analysis is done for the velocity integrated maps. The results are given in both last columns

telescope	transition	telescope HPBW	map: # pixels	sampling	σ_β/σ_n [1]	$\beta = d_\Delta + 2$	fit range lag L [pc]
CfA 1.2 m	^{12}CO $J = 1 \rightarrow 0$	$8.7'$	92×128	$8'$	7.97	2.61 ± 0.16	0.75–6.0
KOSMA 3 m	^{12}CO $J = 2 \rightarrow 1$	$2.2'$	48×62	$1'$	6.44	3.05 ± 0.22	0.13–0.6
FCRAO 14 m	^{13}CO $J = 1 \rightarrow 0$	$0.78'$	160×108	$0.367'$	6.74	3.22 ± 0.15	0.06–0.48
IRAM 30 m	^{12}CO $J = 1 \rightarrow 0$	$0.35'$	48×64	$0.125'$	6.31	3.29 ± 0.22	0.02–0.07
IRAM 30 m	^{12}CO $J = 2 \rightarrow 1$	$0.175'$	48×64	$0.125'$	3.34	3.25 ± 0.23	0.02–0.07

[1] Ratio of the rms intensity of velocity integrated line maps, integrated over the line (σ_β) and over (the same amount of) signal-free channels (σ_n).

Table 3. Surveys of the ^{13}CO $J = 1 \rightarrow 0$ transition towards molecular cloud complexes, made with the Bell Labs 7 m telescope (Bally 1998, *priv. comm.*). The HPBW of the 7 m telescope at 110 GHz is $100''$

source	adopted distance [pc]	# positions observed	σ_β/σ_n	$\beta = d_\Delta + 2$	fit range lag L [pc]
Perseus/NGC1333	350	33 000	7.28	3.07 ± 0.10	0.31–2.52
Orion A	450	33 000	6.31	2.54 ± 0.05	0.39–7.50
Orion B	415	80 000	5.75	2.68 ± 0.12	0.36–6.92
NGC 2264/Mon OB1	800	19 000	14.82	2.54 ± 0.12	0.93–7.14
Mon R2	950	7 000	5.00	2.76 ± 0.12	0.69–2.16

Δ-variance, we obtain a spectral index of $\beta = 3.47$ for the IRAM ^{12}CO $J = 1 \rightarrow 0$ map, which is significantly larger than the value obtained here using the three-parameter fit, $\beta = 3.29$. For the IRAM ^{12}CO $J = 2 \rightarrow 1$ map we obtain a *smaller* index ($\beta = 3.08$), compared to the $\beta = 3.25$ from the three-parameter fit. Thus, for the IRAM ^{12}CO $J = 2 \rightarrow 1$ map, the deviation of the Δ-variance from a straight line essentially arises from the contribution of noise, while for the IRAM ^{12}CO $J = 1 \rightarrow 0$ map, beam smearing effects dominate. The modification of the spectral index is significant, despite the fact that the influence of beam smearing and noise is confined to small lags. This is a general rule for observed maps with a relatively small dynamical range in linear resolution (some 3000 positions for the IRAM maps). It does not only apply to the Δ-variance, but has to be considered for other methods to quantify the structure, as it is done e.g. for the two-point correlation functions by Miesch & Bally (1994).

It is interesting to note that after the correction of both effects we obtain the same spectral index β for both IRAM maps (within the errors), a result which is not obvious from the uncorrected Δ-variance. This is supported by the results of Falgarone et al. (1998), who note a remarkably constant intensity ratio of the ^{12}CO $J = 2 \rightarrow 1$ to ^{12}CO $J = 1 \rightarrow 0$ across the maps.

7. Summary

We presented a detailed study of the Δ-variance as a tool to determine the power law power spectral index β of 2-dimensional intensity distributions, such as observed maps of the ISM. We compared algorithms to determine the Δ-variance for discretely sampled data in the Fourier domain and in the spatial domain. They were verified using *fBm-fractals*, artificially generated structures with well defined properties, providing a realistic representation of observed molecular cloud images. A study of the accuracy and the limitation of the Δ-variance analysis was given.

Edge effects were found to be important for maps which do not trace the full spatial extent of the emission, as it is typically the case for most high resolution observations. We demonstrated that the influence of edge effects can be significant for methods which quantify the structure using the Fourier transform of the image. For images with $\beta > 3$ the index determined for a sub-set is significantly smaller than that of the original image. In contrast, the Δ-variance determined in the spatial domain provides a reliable estimate for the index β. For small maps, the accuracy of the index β is limited by the edge effects, and we estimated the minimum required map size to be 32×32 pixels.

A leading order approximation was deduced for the influence from the beam smearing and white noise. This

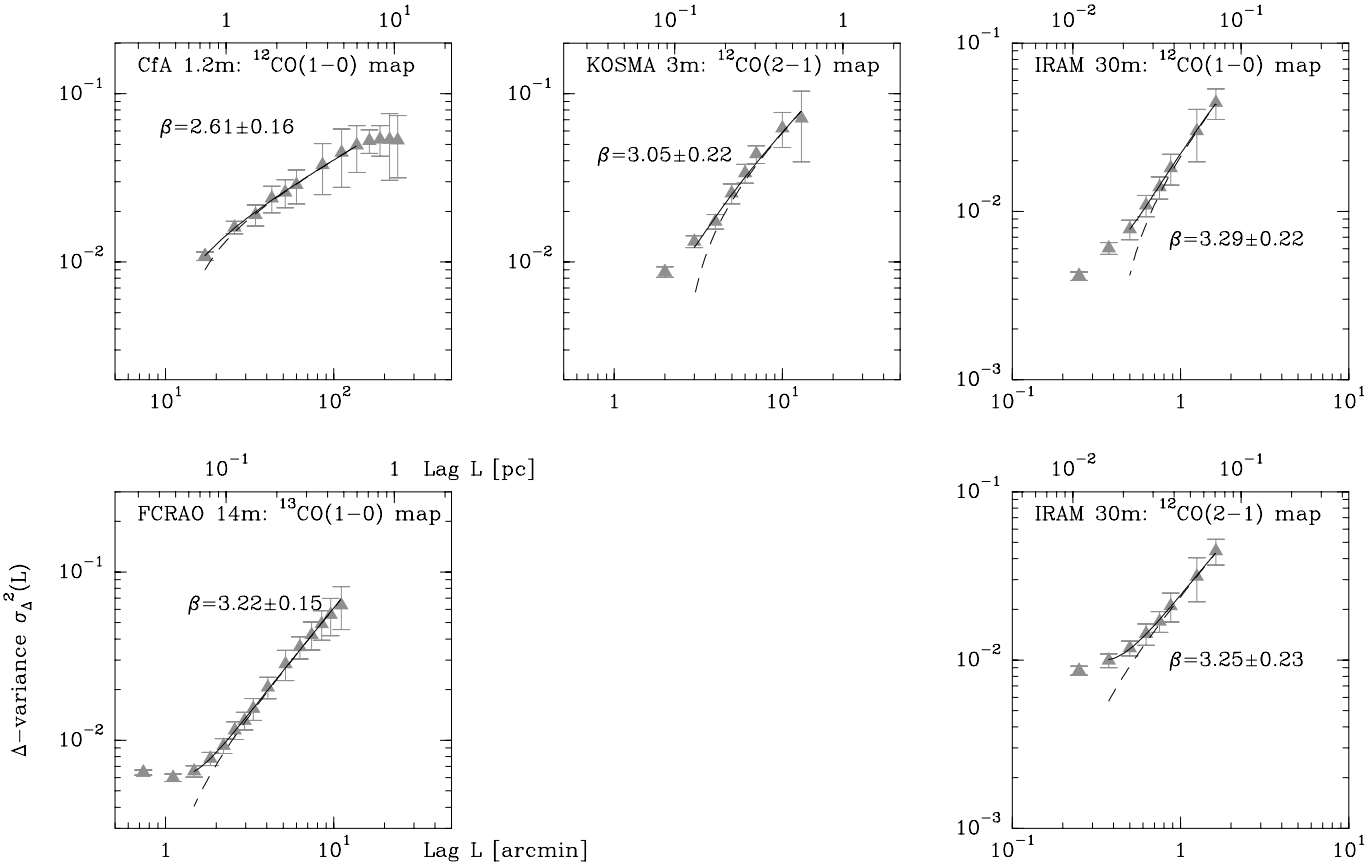

Fig. 9. Δ-variance of the velocity integrated spectral line maps shown in Fig. 8. The solid line gives the result of a χ^2-fit to the data, using the Δ-variance model of Eq. (15). The power spectral index β obtained from this fit is indicated in each panel. The dashed line shows the Δ-variance corrected for white noise and the turnover of the dashed line toward smaller lags (divergence from a straight line) indicates the influence of the telescope beam

enables us to study the Δ-variance for a larger range of lags, and for small maps containing less than 64×64 pixels. For the latter, we found that a significant fraction of the Δ-variance is affected by noise and beam smearing, resulting in a systematic error if no correction is done.

We applied the Δ-variance to several observed CO maps, including surveys of giant molecular clouds made with the Bell Labs 7 m telescope and observations toward the Polaris Flare/MCLD 123.5+24.9, a translucent cloud at high Galactic latitudes. We found that the spatial structure of the velocity integrated maps is well characterized by a power law power spectrum. For linear scales $\gtrsim 0.5$ pc, the spectral index is remarkably uniform ($2.5 < \beta < 2.8$) for different clouds (quiescent/star forming) and tracers with different optical depths (^{12}CO and ^{13}CO $J = 1 \rightarrow 0$). Significantly larger indices ($\beta > 3$) are found for the ^{13}CO $J = 1 \rightarrow 0$ map of Perseus/NGC 1333 and observations made at higher spatial resolution toward MCLD 123.5+24.9, suggesting that the structure is smoother at scales $\lesssim 0.5$ pc. At present, it is not clear whether this reflects some peculiar properties of the high latitude translucent cloud, optical depth effects or the physical processes responsible for the dissipation of the non-thermal motions in molecular cloud cores.

In forthcoming papers we will extend the studies to individual channel maps to establish links between the velocity and spatial structure (Bensch et al., in prep.) and investigate the influence of optical depth effects (Ossenkopf et al., in prep.). An application of the Δ-variance to 3-dimensional density structures (and their 2-dimensional projections) generated by numerical simulations of magneto-hydrodynamic turbulence is presented by MacLow & Ossenkopf (2000) and Ossenkopf & MacLow (2000).

Appendix A: Δ-variance for images with a power law power spectrum

Consider an image $s_\beta = s_\beta(x, y)$ with a power law power spectrum

$$P_{s_\beta}(k) = P_{s_\beta,0} \begin{cases} 1 & 0<k<k_l \\ \frac{k^{-\beta}-k_h^{-\beta}}{k_l^{-\beta}-k_h^{-\beta}} & k_l \le k < k_h \\ 0 & k>k_h \end{cases} , \qquad (A.1)$$

and a spectral index in the range $0 \le \beta \le 4$. Here, $k = (k_x^2+k_y^2)^{1/2}$ is the spatial frequency, and k_l, k_h the low and high frequency cutoffs. For a map with $n \times n$ pixels and a

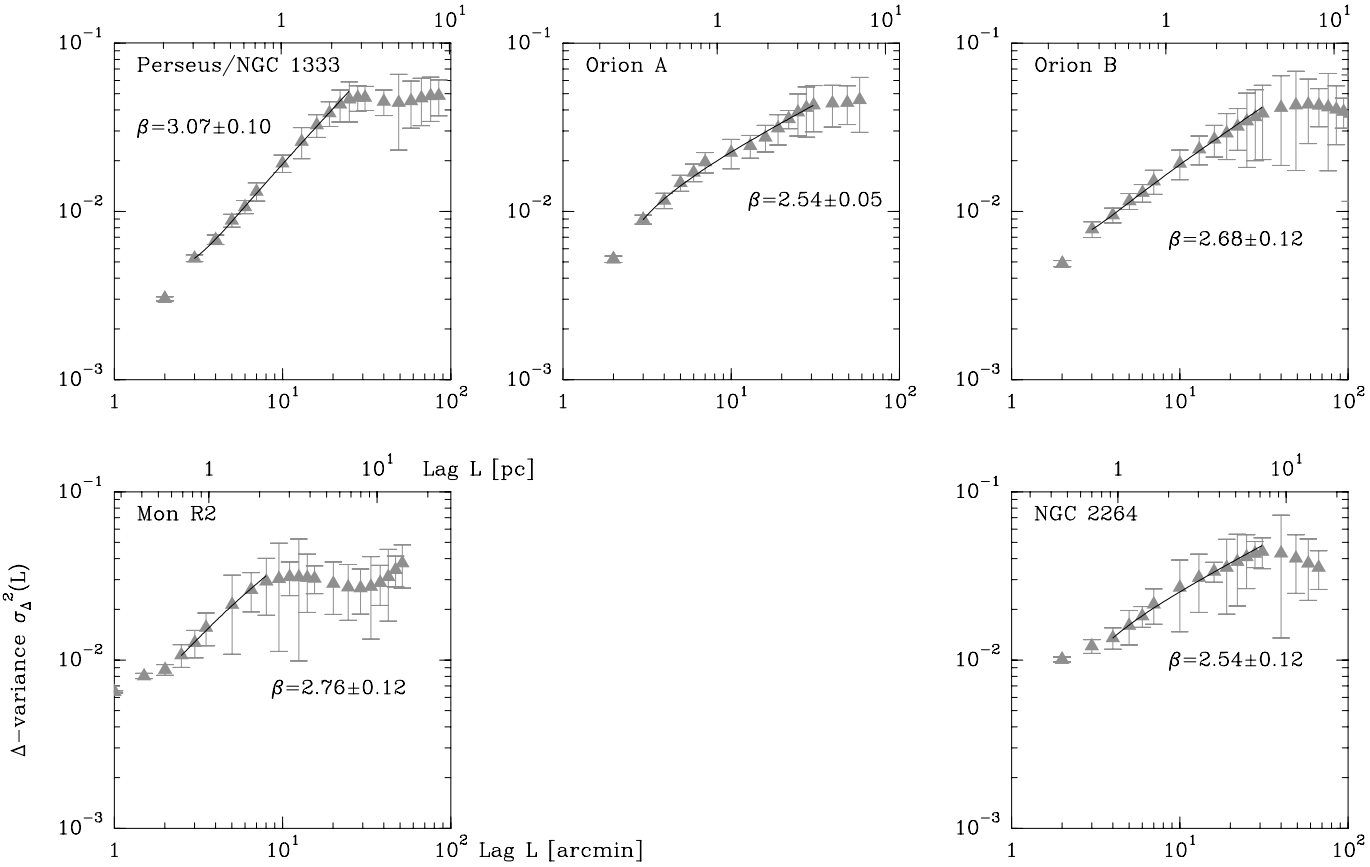

Fig. 10. Bell Labs 7 m surveys: Δ-variance of the velocity integrated spectral line maps. The result of the three-parameter fit is shown as solid line. The flattening of the Δ-variance towards larger scale is due to the finite spatial extent of the emission, which is much smaller than the linear size of the map

Table A1.

β	0.5	1.0	1.5	2.0	2.5	3.0	3.5	4.0
c_β	4.237	0.765	0.146	$0.132\,(\ln n)^{-1}$	0.033	0.037	0.033	0.029

sampling of $\Delta x = \Delta y$, the cutoffs are $k_\mathrm{h} \approx (2\,\Delta x)^{-1}$ and $k_\mathrm{l} \approx (2\,n\Delta x)^{-1}$, respectively.

Assuming $\langle s_\beta \rangle_{x,y} = 0$, the Δ-variance is given by a power law,

$$\sigma_\Delta^2(L)/\sigma_\beta^2 = \begin{cases} \frac{9}{4\pi^3}(k_\mathrm{h}L)^{-2}, & \beta{=}0, \quad (2\pi k_\mathrm{h})^{-1} \ll L \\ c_\beta (2\pi k_\mathrm{h} L)^{\beta-2}, & 0{<}\beta{\leq}2, \quad (2\pi k_\mathrm{h})^{-1} \ll L \ll (2\pi k_\mathrm{l})^{-1} \\ c_\beta (2\pi k_\mathrm{l} L)^{\beta-2}, & 2{<}\beta{<}4, \quad L \ll (2\pi k_\mathrm{l})^{-1} \end{cases}, \quad \text{(A.2)}$$

where σ_β^2 is the integral over the power spectrum and c_β is deduced in the Appendix C of Paper I. The c_β include integrals of squared, first order Bessel functions, which in general do not allow manipulation into a closed form. The evaluation of c_β was done numerically for discrete values of β Table A1.

Appendix B: The influence of the beam smearing: leading order approximation of the Δ-variance

Consider an image with a power law power spectrum given by (Eq. (A.1)). The beam convolved image is then given by $s_\mathrm{B} = s_\beta * B$, where we assume a Gaussian telescope beam B with $\iint B\,\mathrm{d}x\mathrm{d}y = 1$. For small spatial frequencies $k \ll (2\,\ln 2)^{1/2}/(\pi\theta_\mathrm{mb})$, the power spectrum of the Gaussian can be approximated by both first terms of the series expansion, $|\tilde{B}(k)|^2 \approx 1 - \frac{\pi^2\theta_\mathrm{mb}^2}{2\ln 2}k^2$, where θ_mb is the HPBW of the Gaussian. Thus, in leading order approximation, the power spectrum of the beam convolved image is the power spectrum of the original image, plus an additive correction term,

$$P_{\mathrm{s_B}} - P_{\mathrm{s}_\beta} \approx -P_\mathrm{corr} = -P_{\mathrm{s}_\beta}\,\frac{\pi^2\theta_\mathrm{mb}^2}{2\ln 2}\,k^2.$$

The integral of the power spectrum P_corr gives

$$\sigma_\mathrm{corr}^2 = P_{\mathrm{s}_\beta,0}\,\frac{\pi^3\theta_\mathrm{mb}^2}{4\,\ln 2}\,k_\mathrm{l}^4\,\frac{\beta}{\beta-4}\,\frac{1-(k_\mathrm{l}/k_\mathrm{h})^{\beta-4}}{1-(k_\mathrm{l}/k_\mathrm{h})^\beta} \quad \text{(B.1)}$$

and its Δ-variance is given by $\sigma^2_{\Delta,\mathrm{corr}}(L) = \frac{1}{2\pi} \times \iint P_{\mathrm{corr}} \, |\tilde{\odot}_L|^2 \, \mathrm{d}k_x \mathrm{d}k_y$. Following Paper I, this is

$$\sigma^2_{\Delta,\mathrm{corr}}(L)/\sigma^2_{\mathrm{corr}} = \frac{2\,(\beta-2)}{\beta}\, c_{\beta-2}\, (2\pi k_{\mathrm{h}} L)^{\beta-2} \qquad \text{(B.2)}$$

for lags $(2\pi k_{\mathrm{h}})^{-1} \ll L \ll (2\pi k_{\mathrm{l}})^{-1}$. Thus, the Δ-variance of the beam convolved image can be approximated by

$$\begin{aligned} \sigma'^2_{\Delta}(L) \;&\approx\; \sigma^2_{\Delta} - \sigma^2_{\Delta,\mathrm{corr}} \\ &=\; \sigma^2_{\Delta}(L) \left[1 - K_\beta \left(\frac{L}{\theta_{\mathrm{mb}}} \right)^{-2} \right], \end{aligned} \qquad \text{(B.3)}$$

where σ^2_{Δ} is the Δ-variance of the original image and

$$K_\beta = \frac{1}{8 \ln 2} \frac{c_{\beta-2}}{c_\beta} \frac{(\beta-2)^2}{\beta(4-\beta)} \frac{1-(k_{\mathrm{l}}/k_{\mathrm{h}})^{4-\beta}}{1-(k_{\mathrm{l}}/k_{\mathrm{h}})^{\beta-2}}. \qquad \text{(B.4)}$$

The ratio of the low to the high frequency cutoff $k_{\mathrm{l}}/k_{\mathrm{h}}$ is $\sim n^{-1}$ for maps with $n \times n$ positions. The factor $\frac{1-(k_{\mathrm{l}}/k_{\mathrm{h}})^{4-\beta}}{1-(k_{\mathrm{l}}/k_{\mathrm{h}})^{\beta-2}}$ on the right hand side of Eq. (B.4) is then significant only for $\beta \lesssim 2.5$ and $\beta \gtrsim 3.5$, where it corresponds to a correction of larger than 20%. For β between 2.5 and 3.5 we can use the approximation $\frac{1-(k_{\mathrm{l}}/k_{\mathrm{h}})^{4-\beta}}{1-(k_{\mathrm{l}}/k_{\mathrm{h}})^{\beta-2}} \approx 1$. With the additional assumption of $\Delta x = 0.5\theta_{\mathrm{mb}}$, the Δ-variance is approximated by

$$\sigma'^2_{\Delta}(L) \approx \sigma^2_{\Delta}(L) \, \left[1 - K'_\beta (L/\Delta x)^{-2} \right]$$

for lags $(L/\Delta x) \gg (2 \ln 2)^{-1/2}$, where

$$K'_\beta \approx \frac{1}{2 \ln 2} \frac{c_{\beta-2}}{c_\beta} \frac{(\beta-2)^2}{\beta(4-\beta)}, \qquad \text{(B.5)}$$

using the coefficients from Table A1.

Acknowledgements. We like to thank John Bally for providing the surveys made with the AT&T Bell Labs 7 m telescope and Paul Goldsmith for helpful discussions and comments on the manuscript. F. B. wishes to thank Mark Heyer for the support and the assistance during the observing run at FCRAO 14 m telescope. The KOSMA 3 m radio telescope at the Gornergrat-Süd Observatory is operated by the University of Cologne and supported by the Deutsche Forschungsgemeinschaft through grants SFB-301 and SFB-494, as well as special funding from the Land Nordrhein-Westfalen. The receiver development was partly funded by the Bundesminister für Forschung and Technologie. The Observatory is administered by the Internationale Stiftung Hochalpine Forschungsstationen Jungfraujoch und Gornergrat, Bern. This research has made use of NASA's Astrophysics Data System Abstract Service.

References

Allan, D. W. 1966, Proc. IEEE, 54, 221
Bally, J., Langer, W. D., Stark, A. A., & Wilson, R. W. 1987, ApJ, 312, L45
Bally, J., Stark, A. A., Wilson, R. W., & Langer, W. D. 1989, in The Physics and Chemistry of Interstellar Molecular Clouds, mm and sub-mm Observations in Astrophysics, ed. G. Winnewisser, & J. T. Armstrong (Springer: Berlin), 81
Bensch, F. 1998, Ph.D. Thesis, Universität zu Köln
Barnes, J. A., Chi, A. R., Cutler, L. S., et al. 1971, IEEE Transactions on Instrumentation and Measurement, vol. IM-20, No. 2, 105
Beech, M. 1986, Astrophys. Space Sci., 133, 193
Bracewell, R. N. 1986, The Fourier Transform and its Applications, 2nd edition (McGraw-Hill, Singapore)
Crovisier, J., & Dickey, J. M. 1983, A&A, 122, 282
Elmegreen, B. G., & Falgarone, E. 1996, ApJ, 471, 816
Falgarone, E., Phillips, T. G., & Walker, C. K. 1991, ApJ, 378, 186
Falgarone, E., & Phillips, T. G. 1996, ApJ, 472, 191
Falgarone, E., Panis, J.-F., Heithausen, A., et al. 1998, A&A, 331, 669
Green, D. A. 1993, MNRAS, 262, 327
Heithausen, A., & Thaddeus, P. 1990, ApJ, 353, L49
Heithausen, A. 1999, A&A, 349, L53
Heyer, M. H., & Terebey, S. 1998, ApJ, 502, 265
Houlahan, P., & Scalo, J. 1990, ApJS, 72, 133
Kleiner, S. C., & Dickman, R. L. 1984, ApJ, 286, 255
Kogut, A., & Hinshaw, G. 1996, ApJ, 464, L39
Kramer, C., Stutzki, J., Röhrig, R., & Corneliussen, U. 1998, A&A, 329, 249
Langer, W. D., Velusamy, T., Kuiper, T. B. H., et al. 1995, ApJ, 453, 293
MacLow, M.-M., & Ossenkopf, V. 2000, A&A, 353, 339
Miesch, M. S., & Bally, J. 1994, ApJ, 429, 645
Ossenkopf, V., & MacLow, M. M. 2000, submitted to A&A
Padoan, P., Juvela, M., Bally, J., & Nordlund, Å. 1998, ApJ, 504, 300
Peitgen, H. O., & Saupe, D. 1988, The Science of Fractal Images (Springer, New York)
Pérault, M., Falgarone, E., & Puget, J. L. 1986, A&A, 157, 139
Rosolowsky, E. W., Goodman, A. A., Wilner, D. J., & Williams, J. P. 1999, ApJ, 524, 887
Scalo, J. M. 1984, ApJ, 277, 556
Scalo, J. M. 1990, in Physical Processes in Fragmentation and Star Formation, ed. R. Capuzzo-Doletta, et al. (Dordrecht: Reidel), 151
Smoot, G. F., Bennett, C. L., Kogut, A., et al. 1992, ApJ, 396, L1
Stanimirovic, S., Staveley-Smith, L., Dickey, J. M., Sault, R. J., & Snowden, S. L. 1999, MNRAS, 302, 417
Stutzki, J., & Güsten, R. 1990, ApJ, 356, 513
Stutzki, J. 1999, in The Physics and Chemistry of the Interstellar Medium, Proceedings of the 3rd Cologne-Zermatt Symposium, ed. V. Ossenkopf, et al. (Herdecke: GCA-Verlag), 203
Stutzki, J., Bensch, F., Heithausen, A., Ossenkopf, V., & Zielinsky, M. 1998, A&A, 336, 697, Paper I
Tegmark, M. 1996, ApJ, 464, L35
Vogelaar, M. G. R., & Wakker, B. P. 1994, A&A, 291, 557
Williams, J. P., de Geus, E. J., & Blitz, L. 1994, ApJ, 428, 693
Williams, J. P., Blitz, L., & McKee, C. F. 2000, in Protostars and Planets IV, ed. V. Mannings, et al. (Tucson: University of Arizona Press), 97
Wright, E. L., Bennett, C. L., Górski, K., Hinshaw, G., & Smoot, G. F. 1996, ApJ, 464, L21
Zagury, F., Boulanger, F., & Banchet, V. 1999, A&A, 352, 645
Zimmermann, T., & Stutzki, J. 1992, Phys. A, 191, 79
Zimmermann, T., & Stutzki, J. 1993, Fractals, 1, 930